Top Catal (2017) 60:1744–1753
DOI 10.1007/s11244-017-0851-8

ORIGINAL PAPER

Probing Oxide Reduction and Phase Transformations at the Au-TiO_2 Interface by Vibrational Spectroscopy

Anna Pougin[1] · Alexander Lüken[1] · Christina Klinkhammer[2] · Dennis Hiltrop[1] · Max Kauer[3] · Katharina Tölle[1] · Martina Havenith-Newen[2] · Karina Morgenstern[3] · Wolfgang Grünert[1] · Martin Muhler[1] · Jennifer Strunk[4,5,6]

Published online: 17 August 2017

Abstract By a combination of FT-NIR Raman spectroscopy, infrared spectroscopy of CO adsorption under ultra-high vacuum conditions (UHV-IR) and Raman spectroscopy in the line scanning mode the formation of a reduced titania phase in a commercial Au/TiO_2 catalyst and in freshly prepared Au/anatase catalysts was detected. The reduced phase, formed at the Au-TiO_2 interface, can serve as nucleation point for the formation of stoichiometric rutile. Ti_nO_{2n-1} Magnéli phases, structurally resembling the rutile phase, might be involved in this process. The formation of the reduced phase and the rutilization process is clearly linked to the presence of gold nanoparticles and it does not proceed under similar conditions with the pure titania sample. Phase transformations might be both thermally or light induced, however, the colloidal deposition synthesis of the Au/TiO_2 catalysts is clearly ruled out as cause for the formation of the reduced phase.

Keywords TiO2 · Anatase · Rutile · Gold nanoparticles · CO oxidation · Raman spectroscopy · UHV-FTIR

1 Introduction

As a non-toxic, abundantly available semiconductor with band edge positions thermodynamically suitable for overall water splitting, TiO_2 is the single most frequently used material in photocatalysis [1] At the same time, it has a long history of application in classical heterogeneous catalysis, both as catalyst and as support material. In this respect, the combination with gold nanoparticles as catalyst or cocatalyst is very common, for example in low temperature CO oxidation [2, 3] or for the selective oxidation of alcohols [4–7]. Since TiO_2 can commonly exist in different crystal structures, with anatase and rutile being the two most common and most studied ones [1], there has been much debate about the (photo)catalytic properties of either of them. In photocatalysis usually electron transport [8, 9] the electronic structure [10], or the properties of the respective facets are discussed [11–13]. The combination of both anatase and rutile is of further interest due to the widespread use of the commercial TiO_2 material P25, which in its as-made state consists of a mixture of about 80% anatase and 20% rutile [14]. In many studies this material has demonstrated superior performance over the separate crystal modifications, probably based on charge carrier separation processes and the associated longer charge carrier lifetime [15, 16].

Anna Pougin and Alexander Lüken contributed equally to this work.

Electronic supplementary material The online version of this article (doi:10.1007/s11244-017-0851-8) contains supplementary material, which is available to authorized users.

✉ Jennifer Strunk
jennifer.strunk@catalysis.de

[1] Lehrstuhl für Technische Chemie, Ruhr-Universität Bochum, Universitätsstr. 150, 44801 Bochum, Germany

[2] Lehrstuhl für Physikalische Chemie I, Ruhr-Universität Bochum, Universitätsstr. 150, 44801 Bochum, Germany

[3] Lehrstuhl für Physikalische Chemie II, Ruhr-Universität Bochum, Universitätsstr. 150, 44801 Bochum, Germany

[4] Max-Planck-Institut für Chemische Energiekonversion, Stiftstr. 34-36, 45470 Mülheim a. d. Ruhr, Germany

[5] Center for Nanointegration Duisburg-Essen (CENIDE), Carl-Benz-Str. 199, 47057 Duisburg, Germany

[6] Present Address: Leibniz-Institut für Katalyse e.V. an der Universität Rostock (LIKAT), Albert-Einstein-Str. 29a, 18059 Rostock, Germany

With the deposition of noble metals such as gold on the TiO_2 surface, the situation becomes even more complicated, because the resulting metal–metal oxide system displays a very unique electronic structure [17]. Furthermore, the catalytically active sites could be located on the gold nanoparticles, on the support, or at the metal–semiconductor interface [3–5]. The question arises as to whether nanoparticles supported on the different TiO_2 modifications anatase and rutile differ in their catalytic behavior, and whether the support actually remains unchanged after noble metal deposition. In this respect, temporal changes in gold-titania catalysts are well-known to occur, and the common recommendation among researchers is to store those catalysts under the exclusion of light and at low temperatures [18]. The occurrence of photo- and/or thermally induced processes is thus beyond doubt, although no consensus on the nature of those processes has been reached. Phase transitions to the thermodynamically stable rutile structure have been proposed to occur at low temperature and possibly induced by light stimulus [19–21]. In this respect, the deliberate phase transformation of anatase to rutile has recently been brought about in Au/TiO_2 nanoparticulate films by laser processing [21, 22]. Both a laser with wavelength in the visible (532 nm) and the UV range (355 nm) were able to inflict structural changes in Au/TiO_2, but only the UV laser could induce similar changes in nanoparticulate TiO_2 alone. The authors in Refs. [21, 22] concluded that the process was photothermally induced. A darkening of the sample was observed in their work, possibly associated with a reduction or distortion of the titania phase, but the Raman spectra showed no indication for titania reduction [22].

The active structure of the Au-TiO_2 interface has often been hypothesized to be an oxygen-deficient TiO_{2-x} state, possibly characterized by the presence of oxygen vacancies [23, 24], or Ti interstitial atoms [25]. If the interface is present in a reduced state, strong metal-support interactions (SMSI) can also be assumed to occur. Recently, such processes have been evidenced in an Au/TiO_2 catalyst used in CO oxidation, leading to an overgrowth of the gold particles with a thin titania layer [26]. Previously, such processes had also been observed in a related system of photodeposited gold nanoparticles on titania species supported on SBA-15 [27]. However, SMSI effects have been discussed much less for gold catalysts compared to the original Tauster system Pt/TiO_2 [28–30] or Cu/ZnO catalysts [31–33]. Raman spectroscopy is generally very well suited for structural studies of titania, since changes in the phase composition and particle size are well reflected in the spectra [34]. Studies of CO adsorption using infrared spectroscopy are desirable to obtain more information on the (electronic) structure of Au/TiO_2: CO has been found to be an ideal probe molecule to characterize the adsorbing facet of TiO_2 [35, 36], size, shape [37] and charge [38–41] of the Au nanoparticles, the crystal structure of TiO_2 [42], and even the Au-TiO_2 interface [3]. Furthermore, CO oxidation on gold catalysts has been studied extensively over the past two decades [38], yet mostly with a focus on the active state of gold but less attention to the underlying titania phase. In a previous study by some of the authors of this work [38], both TiO_2-supported Au^{3+} ions and Au^0 sites were shown to catalyze CO oxidation, with the former ones acting at very low temperatures and an apparent activation energy of about zero. In this previous work, mixed-phase P25 was used as support and not further structurally characterized [38]. However, in previous studies of photooxidation of CO on TiO_2 single crystal surfaces using reflection–absorption IR spectroscopy (RAIRS), reaction cross sections on anatase TiO_2 (101) have been found to be an order of magnitude larger than those on rutile TiO_2 (110), which has been related to the differences in the lifetime of excited charge carriers [43, 44].

In this contribution, phase transformations at the Au/TiO_2 interface are identified in real catalyst materials, including a commercial gold catalyst. It is demonstrated that already in the first Raman spectra of fresh Au/anatase samples prepared by colloidal deposition the Au-TiO_2 interface has structurally changed significantly. We were able to identify the newly formed structure as a reduced TiO_{2-x} phase, probably of the Magnéli-type Ti_nO_{2n-1}. Due to the structural resemblance between this phase and the rutile structure, it can serve as a nucleation point for an anatase–rutile phase transition. This phase transition can be clearly linked to the presence of gold nanoparticles, because the synthesis procedure alone or rutile impurities in the support are excluded as possible causes. Further evidence for the reduction of the support material, represented by Ti^{3+} species, is obtained by CO adsorption experiments in an ultra-high vacuum infrared spectroscopy (UHV IR) set-up.

2 Experimental

2.1 Samples and Synthesis

One weight percentage of gold nanoparticles of approx. 4 nm diameter were deposited on commercial anatase TiO_2 (specific surface area of ~300 $m^2\ g^{-1}$; material consists of almost round nanoparticles with a diameter of 10–20 nm; *Sachtleben Chemie GmbH*, now: *Huntsman P&A Germany*) and on P25 (specific surface area approximately 50 $m^2\ g^{-1}$; rutile/anatase = 20/80; *Evonik Industries AG*) by the colloidal deposition method as described in Refs. [45–47]. One sample was prepared similarly, but not calcined after the colloidal synthesis (Au/anatase uncalc.). To investigate the role of the chemicals used in the synthesis, anatase blank samples were generated in analogy to the original colloidal deposition method by exposing anatase to the same chemicals at

the same concentrations of chloride, $NaBH_4$, and PVA, but without using $HAuCl_4$. A potential influence of chloride anions in the auric acid precursor was accounted for by the addition of the same chloride concentration using NaCl. One part of this anatase sample was calcined according to the established method at 250 °C, the other was simply dried to study a possible influence of the heat treatment on the phase composition (blank "Au/anatase" calc. and uncalc.) The commercial AUROlite™ catalyst was used as reference. It was provided by STREM Chemicals Inc. and was not treated apart from being finely ground to powder in a mortar for about 10 min. The average size of the gold nanoparticles is in the range of 2–3 nm [4, 48]. Details of the calculation of the average distance of the gold nanoparticles can be found in the supplementary information.

2.2 Raman Spectroscopy

Unless otherwise noted, Raman spectra were measured with a confocal Raman microscope (WITec alpha300 RAS, Ulm, Germany). The laser radiation was coupled into the microscope by a single mode optical fiber. A 20× objective (Zeiss EC EPIPLAN, NA = 0.4) was used to focus the laser beam on the sample. The scattered light was collected by the same objective and was transmitted to the spectrometer via a multimode optical fiber. The optical fibers provide the pinholes for the confocal setup.

For irradiation of the Au/anatase sample a frequency-doubled Nd: YAG laser (operating at 40 mW) with an excitation wavelength of 532 nm and a multimode optical output fiber with a core diameter of 50 µm were used. The spectrometer unit (UHTS300) was equipped with a diffraction grating (600 grooves per mm) and a back-illuminated electron multiplying charge-coupled device (1600 × 200 pixels, cooled to −60 °C) achieving a spectral resolution of 3 cm^{-1}. Line scans were measured with a total integration time of 15 s per spectrum.

For the AUROlite™ sample a single frequency diode laser with a wavelength of 785 nm (operating at 25 mW) and a multimode optical output fiber with a core diameter of 100 µm were used. The 785 nm laser was chosen for this catalyst to suppress fluorescence that overshadowed the measurements with the 532 nm laser for this compound. The spectrometer unit consisted of a diffraction grating (300 grooves per mm) and a back-illuminated deep depletion charge-coupled device camera (1024 × 127 pixels, cooled to 60 °C). Line scans were acquired with a total integration time of 0.427 s per spectrum. A complete line scan including two hundred spectra migrates across a distance of 200 µm. The starting point of each line scan was picked randomly. From the first point on the Raman laser analyzed spots with a distance of 1 µm. The diameter of the laser was estimated to be 0.7 µm for 532 nm and 1 µm for the 785 nm laser ((FWHM) Gaussian profile).

Furthermore, Raman spectra without distinct localization of the laser were recorded on a Thermo Scientific FT-Raman module for a NEXUS spectrometer with an NIR light source (1064 nm) operated at a nominal power input of 0.5 W. A cut-off filter at 2000 cm^{-1} was used to suppress fluorescence most likely caused by the presence of Au nanoparticles. Spectra were recorded using 500 scans with a spectral resolution of 4 cm^{-1}.

2.3 UHV-IR Spectroscopy

All spectra were recorded in transmission mode by a Bruker VERTEX 80v IR spectrometer with a novel UHV system (PREVAC) connected to an UHV apparatus which is described elsewhere [49]. The tested Au/anatase sample was pretreated by in situ annealing at 500 K for 1 h. For the first CO dosing the sample was pretreated at 500 K for 60 min in ultra-high vacuum, then CO was added stepwise to a pressure of 10^{-7}–10^{-5} mbar in the cell (=first CO dosing), and evacuated afterwards to 10^{-8} mbar. The second CO dosing was performed after the sample had been annealed to 300 K and 10^{-10} mbar, then CO was added again stepwise until a pressure of 10^{-4} mbar had been reached (=second CO dosing). In the following, O_2 was dosed to yield an overall pressure of 10^{-3} mbar in the cell.

2.4 XRD Analysis

Diffraction patterns were recorded in reflection geometry with an Empyrean θ-θ diffractometer (Panalytical, Almelo) equipped with a copper tube, 0.25° divergent slit, 0.5° antiscatter slit (incident beam), 7.5 mm high antiscatter slit (diffracted beam), incident and diffracted beam 0.04 rad soller slits, and a position sensitive PIXcel-1d detector. The K-β emission line was suppressed by a Ni Filter. For qualitative phase analysis the specimens were scanned in the 5°–80° 2θ range with a step width of 0.0131° and 250 s collection time at ambient temperature.

3 Results and Discussion

3.1 AUROlite™ *Catalyst*

XRD analysis of the commercial AUROlite™ catalyst (See Fig. S1 in Supplementary Information) showed that the titania support consists of both anatase and rutile, with a phase ratio of approximately 80% anatase and 20% rutile, very similar to commercial TiO_2 P25. It is very peculiar, though, that the Raman spectrum of the AUROlite™ catalyst measured in a conventional FT-Raman spectrometer with NIR

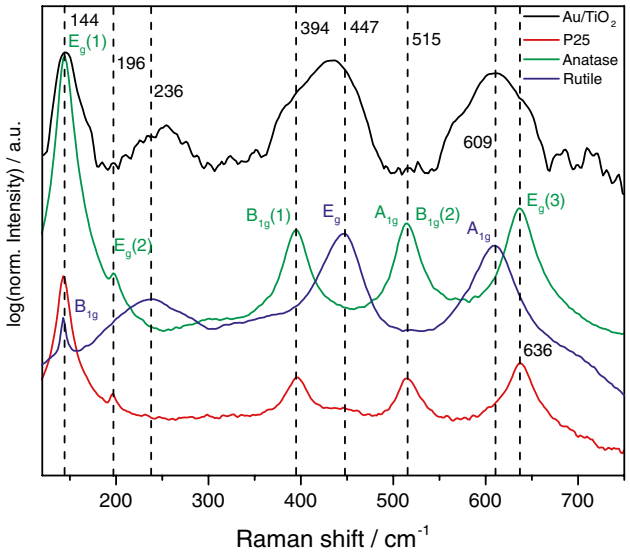

Fig. 1 Raman spectra recorded on a Thermo Scientific FT-Raman module for a NEXUS spectrometer: NIR light source (1064 nm), no distinct localization of the laser possible. The sample name Au/TiO_2 denotes the discussed AUROlite™ sample. The spectrum of the gold catalyst closely resembles the rutile spectrum

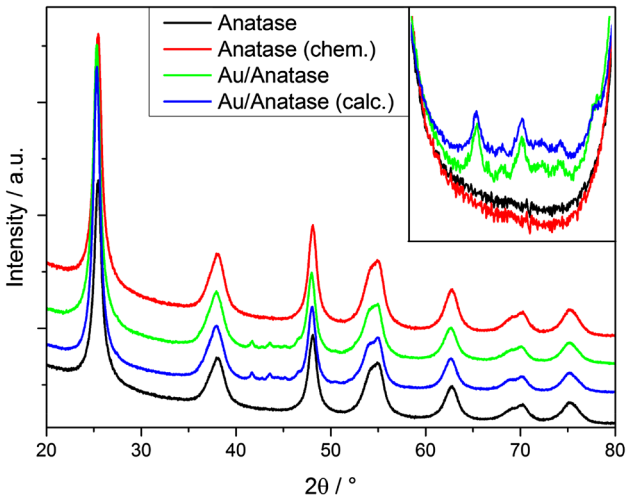

Fig. 2 XRD patterns of the Au/anatase samples (calcined (blue) and uncalcined (green), denoted as Au/anatase (calc.) and Au/anatase respectively), the anatase support chemically treated (denoted as Anatase (chem.), red), and the bare anatase support (denoted as Anatase, black)

laser (1064 nm) resembles much more closely that of a pure rutile reference sample measured in the same spectrometer (Fig. 1). The Raman bands of anatase can only be distinguished as shoulders. It can be ruled out that the preferential observation of the rutile phase is caused by the given measurement conditions: In the mixed-phase material P25 with similar phase composition it is the anatase phase rather than the rutile phase which can be clearly identified (Fig. 1). The obvious pronounced differences in the FT-NIR-Raman spectra of the AUROlite™ catalyst and P25 despite their similarity in phase composition can only be rationalized if either the phase transformation in Au/TiO_2 occurs under irradiation with the Raman laser, or if the presence of gold enhances the signal of rutile selectively, possibly by a surface enhancement effect as used in surface enhanced raman spectroscopy (SERS). Regardless of which of the two causes accounts for the better visibility of rutile in the spectrum of Au/TiO_2, it always implies that rutile occurs in proximity to the gold nanoparticles, because rutile formation does not occur, and/or is not observed, in pure P25 under similar measurement conditions.

3.2 Raman Spectra of Catalysts Prepared by Colloidal Deposition

Initiations of phase transformation processes cannot be studied in depth when starting from a support that already contains both titania phases. So, for all further studies, Au/TiO_2 catalysts with pure anatase support, freshly prepared under dark conditions by the colloidal deposition synthesis were used. For all samples, XRD was used as first indication if the support remained in the anatase phase. As Fig. 2 shows, rutile peaks can neither be detected in the pure anatase support, nor in the blank sample treated according to the colloidal deposition synthesis.

The X-ray diffraction pattern of the Au/anatase sample (Fig. 2), on the contrary, shows small reflections in the region between 40° and 45° 2θ. In this 2θ region, anatase does not feature any diffraction peaks (See Fig. S2 in Supplementary Information). However, rutile (See Fig. S2 in Supplementary Information), brookite and gold [50], as well as Magnéli-type TiO_2 phases [51, 52] display diffraction reflexes between 40° and 45° 2θ. Crystalline gold should only have one signal in this region, though, and it is usually only seen for much higher loadings and larger particles [50]. Due to the absence of any other strong diffraction peaks, or potentially the overlap with those of anatase, we cannot assign those small peaks unambiguously to a certain titania phase by XRD alone. It is clear, however, that the presence of gold induces structural changes. The new diffraction peaks appear both in the calcined and the uncalcined sample, clearly ruling out a decisive effect of the heat treatment during calcination.

In depth structural characterization was thus performed with Raman spectroscopy in the line scanning mode. The full line scan of the Au/anatase sample can be found in Fig. 3a, and the three consecutive spectra 83, 94 and 85 are displayed in Fig. 3b. Spectrum 83 resembles the spectrum of rutile, however, peak positions are shifted with respect to those of stoichiometric rutile, and the intensity in the range

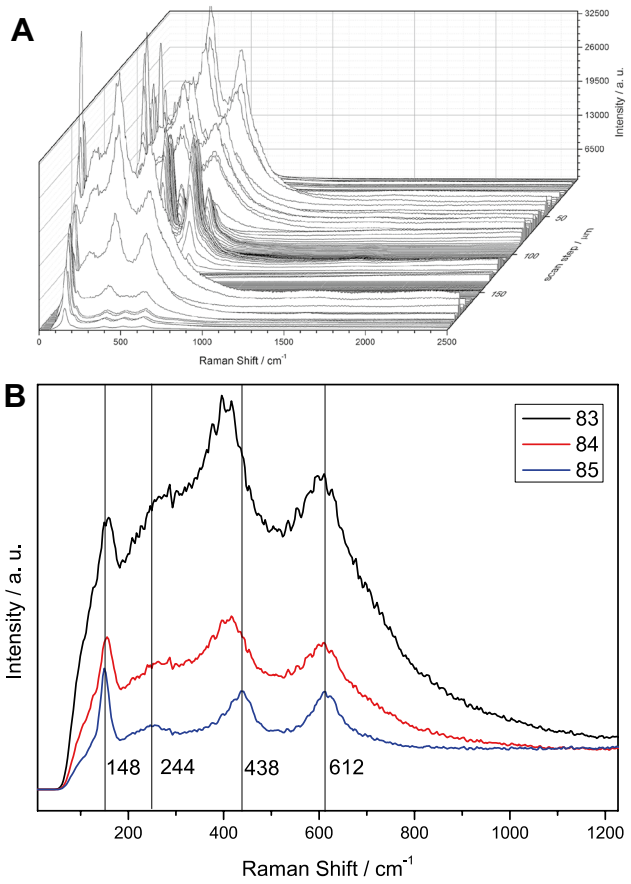

Fig. 3 **a** Two hundred spectra from line scan for the Au/anatase sample with the 532 nm laser. **b** Three selected consecutive Raman spectra from the line scan of Au/anatase, 532 nm laser, measured in the Raman microscope in the line scanning mode

between 100 and 150 cm^{-1} is higher than usually observed for spectra of rutile. So, due to the stronger signal at very low Raman shifts the band at 148 cm^{-1} appears relatively more intense, and it is broadened compared to spectra of stoichiometric rutile (Fig. 1). A broad Raman peak around 140 cm^{-1} has previously been assigned to Ti_nO_{2n-1} Magnéli-type TiO_2 phases [52, 53].

Furthermore, it has been shown that the position of the E_g Raman mode of rutile (447 cm^{-1} in oxidized rutile, Fig. 1) is shifted to lower wavenumbers the more strongly the TiO_2 is reduced [54]. Spectra 83, 84 and 85 can thus be assigned to a reduced rutile phase, probably even containing contributions of a Magnéli-type phase. The spectra measured right after those displayed in Fig. 3b then display the transition to a more and more stoichiometric rutile structure (See Fig. S2 in Supplementary Information). It can be ruled out that the spectrum assigned to the reduced phase just originates from a superposition of the spectra of anatase and rutile phases: In Figure S3, the observed spectrum of the non-stoichiometric phase is compared to spectra of pure rutile, pure anatase, and a superposition spectrum calculated under the assumption of a 1:1 mixture of both phases. It is obvious that the band positions and relative band heights do not match with a simple superposition.

In general, multiple explanations might account for the observation of the rutile phase, namely (1) rutile impurities already present in the anatase support that function as gold anchoring sites, (2) the formation of rutile due to the colloidal deposition synthesis, unrelated to the presence of gold, (3) a phase transformation in the samples related to the presence of the gold nanoparticles, or (4) a phase transformation due to the irradiation with the Raman laser. The first two explanations can be clearly ruled out: The XRD pattern of the pure anatase support (Fig. 2) provides no indication of the presence of a rutile phase, and neither does the diffraction pattern of the blank "Au/anatase" sample that had been subjected to the exact same synthesis procedure, but without the addition of auric acid. It has to be recalled that a potential influence of chloride anions in the auric acid precursor was accounted for by the addition of the same chloride concentration using NaCl. The lack of structural changes in the blank sample clearly rules out the synthesis procedure as cause for the formation of the reduced rutile phase. It might be argued that X-ray diffraction is not sensitive enough to detect the presence of the Magnéli or rutile phase. Consequently, a line scan with the Raman laser of the calcined blank "Au/anatase" sample was performed (See Fig. S4 in Supplementary Information), but no evidence for the presence of any crystal phase except for anatase TiO_2 was found. This also provides evidence that the Raman laser alone does not induce the structural changes in the gold-free samples. We thus conclude that the structural changes are clearly related to the presence of the gold nanoparticles and the electronic structure that occurs at such a Schottky junction. The structural changes in the samples are already evident in the XRD patterns before calcination (Fig. 2), so it is not necessary to treat the samples thermally to induce rutile formation.

While the above discussion already contains valuable insights into structural changes in Au/TiO_2 catalysts, we need to admit that we cannot identify the exact cause for phase transformation at this point. It is possible that chemical processes during colloidal synthesis reduce and structurally transform the TiO_2, but only if gold is present, i.e. close to the interface with the gold nanoparticles. Alternatively, any irradiation with light, i.e. laboratory lighting and/or the Raman laser, might induce the structural changes. Lastly, it is also possible that the thermal energy available under ambient conditions is already sufficient to induce structural changes at the Au/TiO_2 interface.

Based on the method used here, we cannot claim to study separate gold nanoparticles, because the spot size of the Raman laser is much larger than the diameter of the

gold nanoparticles. However, it is peculiar that a sequence of spectra as displayed in Fig. 3b is observed multiple times in the full line scan (Fig. 3a). In order to estimate how many gold particles we would expect in the probed region of the sample, an estimation of the average distance of two gold nanoparticles was derived based the total gold loading (1 wt%), the gold nanoparticle diameter (4 nm) and the surface area of the support (300 m^2/g). Gold nanoparticles were assumed to be hemispheres, which has been suggested as appropriate representation for 2–4 nm sized gold nanoparticles on rutile surfaces [55], also being in agreement with recent HR-TEM observations on Au/TiO_2 catalysts [26]. Our calculation (See Supplementary Information) yielded a distance of about 100 nm, so on the probed area in one line scan (200 spots of ~1 µm diameter), we expect to see approximately 1.6×10^4 Au nanoparticles. If we neglect mutual coverages of TiO_2 powder particles by each other, and further estimate the shape of TiO_2 nanoparticles as simple cubes, then possibly only one-sixth of these nanoparticles are on the top face (~2700 gold nanoparticles). Yet, the strong increase in spectral intensity, tentatively assigned to a plasmonic field enhancement effect due to gold, is observed only four times along the line scan (Fig. 3a). It is well known that probing the direct surroundings of gold nanoparticles with SERS requires a size of the nanoparticles of roughly 20 nm, much larger than the gold nanoparticles used here (~4 nm) [56]. This might explain the deviations of the expected number of gold nanoparticles along the line scan and the appearance of the peculiar spectral features: We assumed an ideal distribution of gold nanoparticles over the surface, and an enhancement of spectral intensity was assumed to be caused by just a single particle. It is possible, though, that multiple gold nanoparticles need to be present as a cluster or a larger arrangement to lead to spectral enhancement. In this respect, larger enhancement effects have been observed for dimers and trimers of metal colloids [57]. Such a cluster of gold nanoparticles might appear just a few times along one line scan.

3.3 Raman Spectra of Commercial Au/TiO_2 Catalyst

Figure 4b shows selected Raman spectra from the line scan of the commercial AUROlite™ catalyst, which demonstrate that phase transformation phenomena also need to be considered for commercial gold catalysts (for the complete line scan see Fig. 4a). The non-stoichiometric rutile phase is also found in this sample (spectra 140 and 149 in Fig. 4b), however, since the support of this catalyst already contained TiO_2 in the rutile structure, it is not possible to determine whether the non-stoichiometric phase was formed from anatase or from rutile, and whether additional phase transitions occur. The observation of both anatase and rutile in the spectra recorded with the 785 nm laser in the Raman

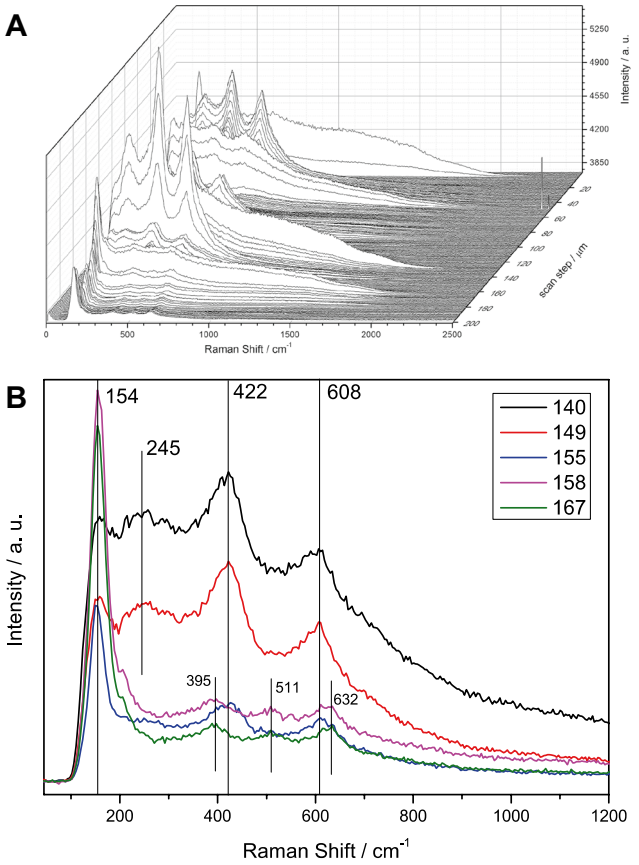

Fig. 4 **a** Two hundred spectra from line scan for the AUROlite™ sample with the 785 nm laser. **b** Selected spectra representing the significant changes along the laser movement found on the AUROlite™ sample; spectrum number 140 and 149 resemble the newly found species of non-stoichiometric TiO_2 developing into a rutile spectrum (155) and further into anatase (158, 167). The spectra in between (not shown) mark transition phases. Spectra measured with 785 nm laser, measured in the Raman microscope in the line scanning mode

microscope as opposed to the observation of almost only rutile in the measurement with the 1064 nm laser is most likely caused by the spatial resolution provided only by the Raman microscope. However, it might also be influenced by differences in penetration/escape depth, thermal effects, and differences in the surface enhancement of the Raman scattering with the two different lasers.

3.4 UHV-IR Spectroscopy of Au/Anatase

The high reducibility of the Au/anatase sample and the reduced titania sites that develop at the interface can be probed very sensitively and under well-defined conditions employing infrared spectroscopy in ultra-high vacuum. It is assumed that the probability for phase transformations induced by irradiation with the probe beam is much reduced in the case of IR spectroscopy compared to the irradiation with a laser in the visible range as applied in

Raman spectroscopy. All UHV-IR spectra were recorded in transmission mode. A spectrum of the sample cleaned by in situ annealing at 500 K for 1 h was used as background for all spectra shown in this contribution.

Figure 5a displays the evolution of bands during the first dosing experiment of CO (for second CO dosing see Fig. S5 in Supplementary Information). The band at 2192 cm^{-1} that shifts to 2189 cm^{-1} with increasing CO pressure represents CO adsorption on coordinatively unsaturated Ti^{4+} sites [41, 58, 59]. This band is the most prominent one, which is easy to rationalize since Ti^{4+} sites are the majority surface sites for CO adsorption on the catalyst. A shift to lower frequencies of the vibration of a probe molecule is often explained with an electron density donating substrate where a stronger back donation of the substrate into the empty π^* orbital of CO takes place [60]. In single crystal experiments on anatase TiO_2 the band has been assigned to CO adsorbed onto Ti^{4+} Lewis sites in (101) and (112) facets in anatase [36]. However, the band positions for CO adsorbed on coordinatively unsaturated Ti^{4+} sites on anatase and rutile are very similar and depend on the exposed surface facet [59], rendering the phase identification of the underlying titania impossible based on this band alone. The band at 2205 cm^{-1} is most probably assignable to CO on a Ti^{4+} site as well, in which the Ti-atom has a higher Lewis acidity and a lower (3- or 4-fold) coordination at kinks or steps [36, 58, 61, 62]. The second most intense band is the one found at 2119 cm^{-1}, which shifts to 2113 cm^{-1} upon increasing CO partial pressure. This band can be assigned to CO adsorbed on three-dimensional Au^0 particles [36, 39, 63].

Already upon the first dosing of CO to the cleaned sample at 93 K, the formation of CO_2 is observed (Fig. 5a), as evidenced by the vibration band of linearly adsorbed CO_2 located at 2349 cm^{-1}. In experiments at higher temperatures CO_2 formation in the Au/TiO_2 system has been explained previously with a Mars–van Krevelen mechanism, in which the oxygen atoms of TiO_2 in close proximity to the gold nanoparticles are used to oxidize CO [3]. The extraction of oxygen from the material, accompanied by the formation of oxygen vacancies, is demonstrated by the vibrational band of CO bound to oxygen vacancies forming at 2140 cm^{-1} [64]. This band is slightly growing in intensity by continued removal of oxygen from the material to supply the oxidation reaction of CO to CO_2. The small band evolving at 2230 cm^{-1} has been assigned to CO_2 interacting with a Au/TiO_2 sample through H-bonds (2235 cm^{-1} in Ref. [38]).

The formation of CO_2 is also accompanied by the appearance of bands characteristic for bidentate carbonate species in the region between 1700 and 1050 cm^{-1} [64] (See Fig. S6 in Supplementary Information). Normally, the vibrational signature for such species is found to be at 1330 and 1560 cm^{-1} [64] or 1320 and 1580 cm^{-1} [65]. Here, however, the strongest bands can be found at 1308 and 1551 cm^{-1}, i.e. shifted by at least nine wavenumbers to lower energy vibrations. It seems likely that the observed shift is indicating a reduced TiO_2 phase.

The shift of the bands of CO adsorbed both on Ti^{4+} sites on TiO_2 (2192–2189 cm^{-1}) [36–41, 64, 66, 67] and on three-dimensional Au^0 particles (2119–2113 cm^{-1}) [39, 41, 63] can also be concluded to originate from the reduction of the material during the oxidation of CO, when oxygen is

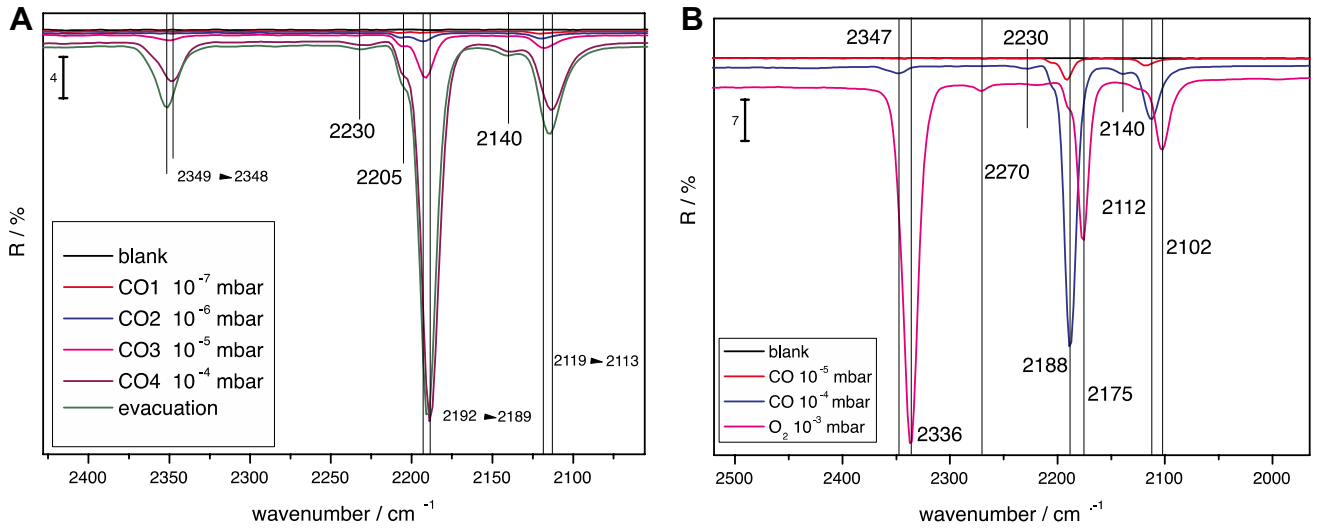

Fig. 5 **a** UHV IR spectra of Au/anatase sample during first CO dosing at 93 K. **b** UHV IR spectra of Au/anatase sample in the region indicative of adsorbed CO_2 and CO during addition of oxygen. This experiment was carried out subsequent to the second CO dosing (See Fig. S5 in Supporting Information) on the same sample as in (**A**) after evacuation to 10^{-8} mbar and annealing at 300 K. The spectra were vertically shifted to facilitate their comparison

extracted from TiO_2. While it is known that the shift of the vibrational modes of adsorbed CO molecules is a function of surface coverage [68], this shift is of minor influence: During the second CO dosing experiment, where CO oxidation does not occur until oxygen was added in the gas phase, the bands indicative of CO adsorption do not shift by more than three wavenumbers with increasing coverage (See Fig. S5 in Supplementary Information).

During evacuation of the cell the band for CO adsorption on Ti^{4+} at 2189 cm^{-1} decreases slightly, while adsorbed CO moieties with bands at other wavenumbers and the bands of adsorbed CO_2 species remain stable (Fig. 5a; See Fig. S6 in Supplementary Information). The evacuation stops the progression of CO oxidation, which causes a slight back shift of all bands to the position at lowest CO content. This slight shift might be caused by a redistribution of adsorbed CO and/or charges in the support upon removal of a few CO and CO_2 molecules from the surface. After evacuation and a second annealing at 300 K hardly any formation of CO_2 is observed during CO dosing (See Fig. S5 in Supplementary Information). Otherwise, spectra in Figure S5 are identical to those in Fig. 5a. The two CO dosing experiments thus confirm that the Au-TiO_2 interface region is highly reducible, so that the oxygen can be used to carry out CO oxidation at extremely low temperature. It should be noted that this is not a catalytic process, but a stoichiometric reaction with oxygen species at the interface. It would be expected that during the second CO dosing some of the CO molecules should preferably bind to coordinatively unsaturated Ti^{3+} sites created in the first dosing experiment. However, it is likely that the carbonates formed as consequence of CO_2 formation preferably saturate those electron-rich sites: CO_2 is a Lewis acid that preferably adsorbs to Lewis basic sites. In this respect, the poisoning effect of carbonates in CO oxidation on Au/TiO_2 is well known, and increased carbonate formation has been observed after reducing pretreatments [69].

After another evacuation procedure oxygen (10^{-3} mbar) was added to the cell (Fig. 5b). As a result, the band assigned to CO adsorption on TiO_2 decreased significantly and shifted from 2188 to 2175 cm^{-1}, suggesting that this is the active species for CO_2 formation under exposure to O_2. The reduction of TiO_2, and potentially also the rutile formation, is again reflected in the band shift: According to Xu et al. [64] the band at 2188 cm^{-1} is characteristic for CO adsorption on oxidized, stoichiometric (110) rutile surfaces and the one at 2175 cm^{-1} (2178 cm^{-1} in Ref. [64]) for adsorption on reduced (110) rutile. The linearly adsorbed CO_2 formed during CO oxidation also indicates TiO_2 reduction during CO oxidation, because the wavenumber for the CO_2 adsorption is at 2336 cm^{-1} instead of 2349 cm^{-1}. The new band appearing at 2270 cm^{-1} during CO oxidation with co-dosed O_2 is at an unusually high wavenumber for CO adsorption onto either Au or TiO_2. It could be another type of CO_2 interacting with Au/TiO_2 through H-bonds (2256 cm^{-1} in Ref. [38]). It might also be explained with CO on positively charged Au [40], since a strong blue-shift is common for CO on positively charged metals. The presence of $Au^{\delta+}$ might indicate that oxygen coordinates to the gold nanoparticles and removes some electron density, for example for superoxide formation [7].

It seems counterintuitive that the characteristic adsorption of CO on reduced TiO_2 (2175 cm^{-1}) can be found while oxygen is dosed, in particular when considering that the band of CO adsorbed at oxygen vacancies (2140 cm^{-1}) cannot be observed anymore. And indeed, in single crystal studies of CO adsorption on perfect and defective rutile surfaces the band of CO adsorbed on the reduced surface was significantly decreased in intensity when oxygen was dosed first [55]. The observation of the band of CO adsorbed on reduced rutile thus must be related to the presence of gold. Apparently, reoxidation of the surface at low temperatures in presence of small amounts of oxygen does not take place when gold is present. The absence of CO bound to oxygen vacancies might be explained in two different ways: Firstly, it has to be noted that oxygen vacancies can only be detected indirectly by the vibration of CO bound to them. So, they might still be present, but blocked by other species, e.g. carbonates, as explained above. Secondly, it is possible that isolated surface oxygen vacancies are refilled by oxygen from the gas phase, while structurally fully established reduced phases containing an excess of electrons (i.e. trapped as Ti^{3+} species) in proximity to the gold nanoparticles remain unaffected. However, the presence of oxygen must make reduced sites such as Ti^{3+} available for CO adsorption, whereas they had been unavailable, for example due to coverage with another adsorbate, in absence of oxygen (Figure S5). CO should preferably bind here, since the interaction with reduced titania is known to be stronger than with perfect surfaces [55, 64]. While we cannot clearly identify the cause for this liberation of Ti^{3+} sites in the present study, it is suggested that a reorganization of the CO_2 bound to the surface might be the reason. In presence of oxygen, much more linearly adsorbed CO_2 is observed (Fig. 5b). Possibly, this change in coordination of the CO_2, from carbonate to linearly adsorbed structure, is caused by a modified charge distribution on the surface due to the concomitant adsorption of oxygen. Adsorbed O_2 as a homoatomic and possibly symmetric molecule would not be detectable by IR spectroscopy. The changes in surface coverage and surface charge distribution then make adsorption sites for CO on Ti^{3+} available. Further studies using electron paramagnetic resonance (EPR) are in progress to identified possible adsorbed superoxide species on Au/TiO_2.

Further, it appears likely that CO molecules adsorbed on such potentially over-reduced larger patches of neighboring Ti^{3+} species cannot be oxidized anymore due to a complete

lack of reactive oxygen in their proximity. In a related manner it has been reported previously that at very low temperatures as applied here, CO adsorbed on Au is not reactive because it is so immobile that it cannot migrate to active Ti^{4+} sites near the Au particles [70]. A similar explanation might also account for CO adsorbed on Ti^{3+}, so no reaction of this species is observed, in spite of the presence of oxygen.

In summary, the observations from UHV-IR support the conclusions based on Raman spectroscopy, suggesting that the TiO_2 phase is extremely easily reducible in presence of Au nanoparticles. Oxygen species from the support thus become mobile and reactive, and they can contribute to CO oxidation at very low temperatures. At the same time, over-reduced patches of a titania phase are formed near the gold particles, presumably having rutile structure, that cannot be fully reoxidized anymore by small amounts of oxygen in the gas phase at low temperature. CO bound to those sites is cannot be oxidized because no reactive oxygen is left in its proximity.

4 Conclusions

In conclusion, the combination of FT-NIR Raman spectroscopy, infrared spectroscopy of CO adsorption under ultra-high vacuum conditions (UHV-IR) and Raman spectroscopy in the line scanning mode allowed identifying an extremely facilitated reduction of TiO_2 in the presence of gold nanoparticles. The high reducibility of the interface region enables the oxygen species to participate in low temperature CO oxidation. The hindered reoxidation, however, leads to CO molecules binding to partially reduced TiO_2 phases without any active oxygen nearby. Raman spectroscopy revealed that the reduced phase has rutile structure. Magnéli-type phases might also be formed. XRD supports the hypothesis that phase transitions of the formerly pure anatase support to Magnéli or (reduced) rutile phases occurs whenever gold is present, potentially thermally initiated and/or photoinduced at low temperatures. The colloidal deposition synthesis was clearly ruled out as cause for the structural rearrangement, which is, instead, clearly linked to the presence of gold nanoparticles.

Such phase transitions were detected in two unrelated Au/TiO_2 samples, a self-prepared one from colloidal deposition and a commercial Au/TiO_2 catalyst. The formation of reduced rutile is observed even if a pure anatase support material is used. Phase transformations are thus likely to be detectable in even more materials when characterized thoroughly. Potentially, previous discussions on the different behavior of Au-modified rutile or anatase TiO_2 have to be revised when a spontaneous reconstruction in proximity to the gold nanoparticles cannot be excluded. Further studies based on Raman spectroscopy are in progress to identify the exact causes of this structural rearrangement at the Au-TiO_2 interface and its role in catalysis and photocatalysis.

Acknowledgements Open access funding provided by Max Planck Society. Part of this work is supported by the Cluster of Excellence RESOLV (EXC 1069) funded by the Deutsche Forschungsgemeinschaft. The authors would like to thank Dr. Thomas Reinecke, Ruhr-University Bochum, for the X-ray diffraction measurements.

References

1. Schneider J, Matsuoka M, Takeuchi M, Zhang J, Horiuchi Y, Anpo M, Bahnemann DW (2014) Chem Rev 114:9919–9986
2. Haruta M (1997) Catal Today 36:153–166
3. Widmann D, Behm RJ (2014) Acc Chem Res 47:740–749
4. Heeskens D, Aghaei P, Kaluza S, Strunk J, Muhler M (2013) Phys Stat Solidi B 250:1107–1118
5. Holz MC, Tölle K, Muhler M (2014) Catal Sci Technol 4:3495–3504
6. Connelly KA, Idriss H (2012) Green Chem 14:260–280
7. Lüken A, Muhler M, Strunk J (2015) Phys Chem Chem Phys 17:10391–10397
8. Di Valentin C, Selloni A (2011) J Phys Chem Lett 2:2223–2228
9. Setvin M, Franchini C, Hao X, Schmid M, Janotti A, Kaltak M, van de Walle CG, Kresse G, Diebold U (2014) Phys Rev Lett 113:086402
10. Luttrell T, Halpegamage S, Tao J, Kramer A, Sutter E, Batzill M (2014) Sci Rep 4:4043
11. Ohno T, Sarukawa K, Matsumura M (2002) New J Chem 26:1167–1170
12. Diebold U, Ruzycki N, Herman G, Selloni A (2003) Catal Today 85:93–100
13. Pan J, Liu G, Lu GQM, Cheng HM (2011) Angew Chem Int Ed 50:2133–2137
14. Ohtani B, Prieto-Mahaney O, Li D, Abe R (2010) J Photochem Photobiol A 216:179–182
15. Du L, Furube A, Yamamoto K, Hara K, Katoh R, Tachiya M (2009) J Phys Chem C 113:6454–6462
16. Tian Y, Tatsuma T (2005) J Am Chem Soc 127:7632–7637
17. Okazaki K, Ichikawa S, Maeda Y, Haruta M, Kohyama M (2005) Appl Catal A 291:45–54
18. Raphulu M, McPherson J, Pattrick G, Ntho T, Mokoena L, Moma J, van der Lingen E (2009) Gold Bull 42:328–336
19. Ricci PC, Carbonaro CM, Stagi L, Salis M, Casu A, Enzo S, Delogu F (2013) J Phys Chem C 117:7850–7857
20. Zhang J, Li M, Feng Z, Chen J, Li C (2006) J Phys Chem B 110:927–935
21. Schade L, Franzka S, Dzialkowski K, Hardt S, Wiggers H, Reichenberger S, Wagener P, Hartmann N (2015) Appl Surf Sci 336:48–52
22. Schade L, Franzka S, Thomas M, Hagemann U, Hartmann N (2016) Surf Sci 650:57–63
23. Lopez N (2004) J Catal 225:86–94
24. Pan X, Xu YJ (2013) Appl Catal A 459:34–40
25. Madsen GKH, Hammer B (2009) J Chem Phys 130:44704

26. Klyushin AY, Greiner MT, Huang X, Lunkenbein T, Li X, Timpe O, Friedrich M, Hävecker M, Knop-Gericke A, Schlögl R (2016) ACS Catal 6:3372–3380
27. Mei B, Wiktor C, Turner S, Pougin A, van Tendeloo G, Fischer RA, Muhler M, Strunk J (2013) ACS Catal 3:3041–3049
28. Tauster SJ, Fung SC, Garten RL (1978) J Am Chem Soc 100:170–175
29. Tauster SJ (1987) Acc Chem Res 20:389–394
30. Tauster SJ, Fung SC, Baker RTK, Horsley JA (1981) Science 211:1121–1125
31. Dahl S, Logadottir A, Egeberg RC, Larsen JH, Chorkendorff I, Törnqvist E, Nørskov JK (1999) Phys Rev Lett 83:1814–1817
32. Grunwaldt JD, Molenbroek A, Topsøe NY, Topsøe H, Clausen B (2000) J Catal 194:452–460
33. Hansen PL (2002) Science 295:2053–2055
34. Meier RJ (2005) Chem Soc Rev 34:743–752
35. Morterra C (1988) J Chem Soc Faraday Trans 84:1617
36. Mino L, Ferrari AM, Lacivita V, Spoto G, Bordiga S, Zecchina A (2011) J Phys Chem C 115:7694–7700
37. Meier DC, Goodman DW (2004) J Am Chem Soc 126:1892–1899
38. Grünert W, Großmann D, Noei H, Pohl MM, Sinev I, De Toni A, Wang Y, Muhler M (2014) Angew Chem Int Ed 53:3245–3249
39. Boccuzzi F, Chiorino A, Manzoli M, Andreeva D, Tabakova T (1999) J Catal 188:176–185
40. Wörz AS, Heiz U, Cinquini F, Pacchioni G (2005) J Phys Chem B 109:18418–18426
41. Boccuzzi F, Chiorino A, Manzoli M (2000) Surf Sci 454–456:942–946
42. Zhao Y, Wang Z, Cui X, Huang T, Wang B, Luo Y, Yang J, Hou J (2009) J Am Chem Soc 131:7958–7959
43. Rohmann C, Wang Y, Muhler M, Metson JB, Idriss H, Wöll C (2008) Chem Phys Lett 460:10–12
44. Xu M, Gao YK, Moreno EM, Kunst M, Muhler M, Wang Y, Idriss Y, Wöll C (2011) Phys Rev Lett 106:138302
45. Holz MC, Kähler K, Tölle K, van Veen AC, Muhler M (2013) Phys Status Solidi B 250:1094–1106
46. Comotti M, Li WC, Spliethoff B, Schüth F (2006) J Am Chem Soc 128:917–924
47. Strunk J, Kähler K, Xia X, Comotti M, Schüth F, Reinecke T, Muhler M (2009) Appl Catal A 359:121–128
48. http://www.strem.com/uploads/resources/documents/autek_copy1.pdf, Accessed Sept. 5, 2016
49. Xu M, Noei H, Buchholz M, Muhler M, Wöll C, Wang Y (2012) Catal Today 182:12–15
50. Yan W, Chen B, Mahurin SM, Schwartz V, Mullins DR, Lupini AR, Pennycook SJ, Dai S, Overbury SH (2005) J Phys Chem B 109:10676–10685
51. Tomaszek R, Pawlowski L, Gengembre L, Laureyns J, Znamirowski Z, Zdanowski J (2006) Surf Coat Technol 201:45–56
52. Li X, Zhu AL, Qu W, Wang H, Hui R, Zhang L, Zhang J (2010) Electrochim Acta 55:5891–5898
53. Watanabe M (2009) Phys Status Solidi B 6:260–263
54. Parker JC, Siegel RW (1990) Appl Phys Lett 57:943–945
55. Diebold U (2003) Surf Sci Rep 48:53–229
56. Xie W, Schlücker S (2014) Rep Prog Phys 77:116502
57. Schlücker S (2014) Angew Chem Int Ed 53:4756–4795
58. Liao LF, Lien CF, Shieh DL, Chen MT, Lin JL (2002) J Phys Chem B 106:11240–11245
59. Noei H, Jin L, Qiu H, Xu M, Gao X, Zhao J, Kauer M, Wöll C, Muhler M, Wang Y (2013) Phys Status Solidi B 250:1204–1221
60. Linsebigler A, Lu G, Yates JT (1995) J Chem Phys 103:9438–9443
61. Mino L, Spoto G, Ferrari AM (2014) J Phys Chem C 118:25016–25026
62. Mino L, Spoto G, Bordiga S, Zecchina A (2012) J Phys Chem C 116:17008–17018
63. Boccuzzi F, Tsubota S, Haruta M (1993) J Electron Spectrosc Relat Phenom 64–65:241–250
64. Xu M, Noei H, Fink K, Muhler M, Wang Y, Wöll C (2012) Angew Chem Int Ed 51:4731–4734
65. Baltrusaitis J, Schuttlefield J, Zeitler E, Grassian VH (2011) Chem Eng J 170:471–481
66. Busca G, Lorenzelli V (1982) Mater Chem 7:89–126
67. Lavalley J (1996) Catal Today 27:377–401
68. Hadjiivanov K, Lamotte J, Lavalley JC (1997) Langmuir 13:3374–3381
69. Saavedra J, Powell C, Panthi B, Pursell CJ, Chandler BD (2013) J Catal 307:37–47
70. Green IX, Tang W, Neurock M, Yates JT Jr (2014) Acc Chem Res 47:805–815